Experimental FSI study of adaptive shock control bumps

Michela Gramola *, Paul J.K. Bruce, Matthew Santer

Department of Aeronautics, Imperial College London, South Kensington, London, SW7 2AZ, UK

HIGHLIGHTS

- The adaptive bumps bifurcate the normal shock into a lambda-shock structure.
- All the bumps tested reduce shock wave unsteadiness.
- The bumps tested reduce wave drag for upstream triple point positions only.
- Adaptive bumps are more robust to small shock oscillations compared to solid bumps.
- The position of the rear leg of the lambda shock exhibits a bistable behaviour.

ARTICLE INFO

ABSTRACT

The shock stabilisation and wave drag reduction potential of a two-dimensional adaptive shock control bump has been studied in the Imperial College supersonic wind tunnel. The bump was modelled as a flexible aluminium alloy plate deformed through spanwise actuation, and several bump heights were tested beneath a Mach 1.4 transonic shock wave. Schlieren images and static pressure readings along the flexible plate allowed the study of the λ-shock structure generated by the bifurcation of the normal shock for a range of shock positions. All bumps tested were found to increase shock stability, but wave drag reduction was only observed for shocks close to the leading edge of the flexible plate. Positive deformations of the flexible plate for downstream shocks are believed to reduce supersonic flow reacceleration, and hence the strength of the rear leg of the λ-shock and wave drag, in comparison to a solid bump with the same shape. The position of the rear leg of the λ-shock was found to exhibit a bistable behaviour, and this is hypothesised to be caused by a complex coupling of aerodynamic and structural instabilities.

© 2018 Published by Elsevier Ltd.

1. Introduction

Shock control bumps (SCBs) are a promising flow control mechanism that can be applied to transonic aerofoils to improve their overall performance. Normal shock waves that occur on the wings of modern transonic aircraft lead to wave drag, and low frequency unsteadiness of this shock is also a potential danger to airframe integrity. As Fig. 1 shows, shock control bumps reduce wave drag by bifurcating the normal shock into a λ-shape, composed of an oblique shock (which compresses the flow more efficiently), followed by a weaker normal shock. The streamwise location of the oblique shock is fixed by the surface curvature at the front of the bump, and this has been reported to have the additional beneficial effect of stabilising the shock (König et al., 2009).

However, the high sensitivity of SCB performance to flow conditions (mainly shock strength, shock position, upstream boundary layer and post-shock adverse pressure gradient) is well known (Bruce and Colliss, 2015). Fig. 2 shows the

---

* Corresponding author.

E-mail addresses: michela.gramola14@imperial.ac.uk (M. Gramola), p.bruce@imperial.ac.uk (P.J.K. Bruce), m.santer@imperial.ac.uk (M. Santer).
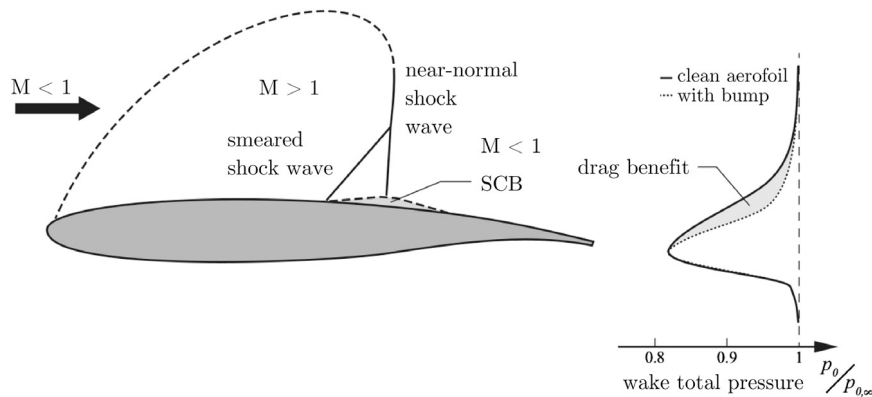
Fig. 1. Shock structure and stagnation pressure recovery for a 2D shock control bump (Bruce and Colliss, 2015).

detrimental effect of flow re-expansion for sub-optimal shock positions. If the shock is too far upstream (Fig. 2(a)), the subsonic post shock flow may reaccelerate to supersonic speeds and terminate with a secondary shock wave. For a downstream shock (Fig. 2(c)), expansion waves increase the strength of the rear leg of the lambda (RLL), which may further bifurcate into a secondary λ-shock. The detrimental effect of reacceleration can be seen from the C_P plots in Fig. 2, where the monotonic two-step pressure rise for the optimum shock position (Fig. 2(b)) is replaced by pressure profiles that show additional (Fig. 2(a)) or stronger (Fig. 2(c)) shocks. In both cases, wave drag increases and the boundary layer becomes more prone to separation. Even if overall drag increases off-design, 2D shock control bumps can still have a positive impact by delaying buffet onset (Eastwood and Jarrett, 2012) and improving shock stability by anchoring the front leg of the lambda shock (König et al., 2009; Bruce and Colliss, 2015).

By allowing geometric variation, adaptive shock control bumps offer the potential for good off-design properties without sacrificing on-design drag saving capabilities. Jinks (2016) carried out wind tunnel experiments and Fluid Structure Interaction (FSI) simulations to study two-dimensional adaptive SCBs, elastically deformed by spanwise actuation. Jinks demonstrated that, when deployed, an actuated adaptive SCB can bifurcate a normal shock and withstand the aerodynamic loading in the same way as a solid bump. When retracted, the normal shock structure is maintained, with only a slight curvature when the shock is positioned above the flexible surface. Rhodes and Santer (2011) presented a structural optimisation of a morphing 3D "default rounded" shock control bump for a variable number of actuation points ($1 \leq n \leq 4$), with the aim of reducing overall drag. They found that continuous actuation increased the accuracy of the morph, but discrete actuation had the ability to capture the required shape, while reducing the complexity and weight of the system, and still maintaining all deformations in the elastic regime. The work from Rhodes and Santer demonstrates the computational and structural challenges associated with realising an adaptive 3D shock control bump compared with a 2D design.

Most studies on shock control bumps have focused on devices placed on unswept wings. However, some computational and experimental studies on 2D SCBs on transonic swept wings were carried out by Kutzbach et al. (2004) and Birkemeyer et al. (2000), who have shown that, unlike for 3D bumps (Jones et al., 2016), both drag performance and optimised shapes do not vary significantly from the corresponding unswept cases.

While studies of the flowfield around solid 2D and 3D shock control bumps of many different geometries are extensive, there is a relative lack of literature on adaptive shock control bumps, in particular under unsteady flow conditions (Bruce and Colliss, 2015). This paper presents an FSI study of 2D actuated shock control bumps, focusing on their wave drag saving and shock stabilisation potential. The flexible nature of adaptive shock control bumps inherently makes this study an aerostructural problem.
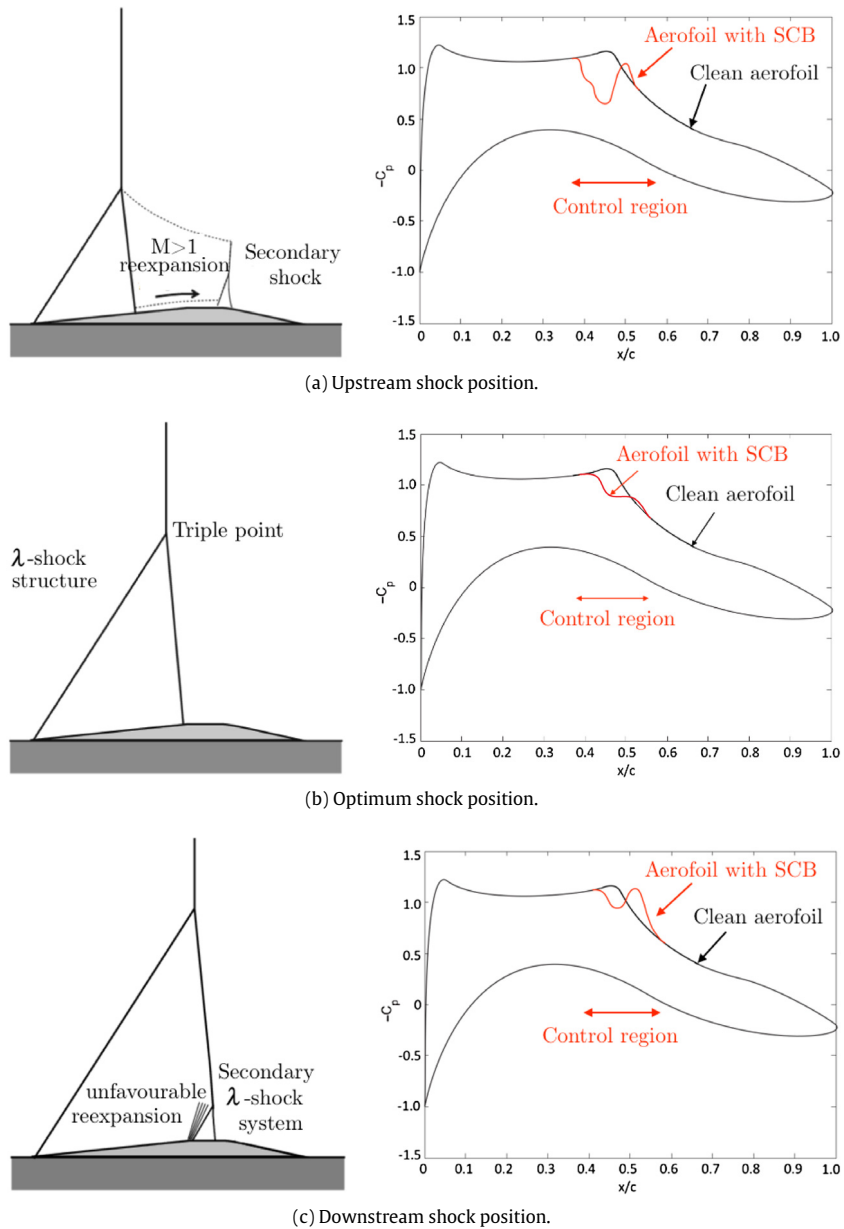
(a) Upstream shock position.

(b) Optimum shock position.

(c) Downstream shock position.

Fig. 2. Effect of shock position on lambda structure (Figures adapted from Ogawa et al. (2008)) and C_P plot.

2. Experimental setup

2.1. Supersonic wind tunnel

Experiments were carried out in the Imperial College supersonic wind tunnel, the main features of which are sketched in Fig. 3. It is a 'blow down' wind tunnel supplied with high pressure compressed air stored at 27 bar in steel tanks of total volume 48 m^3 and exhausting to atmosphere. The working section has a constant cross-sectional area of 150 × 150 mm and it is 727 mm long. The unit Reynolds number in the tunnel is 2.7 × 10^7 m^{-1}, and it is expected to change by less than 3% during a typical run due to stagnation temperature variations. A $M = 1.4$ nozzle is used to generate a shock wave in the test section with a strength that is expected on next generation (laminar flow) transonic wings. The turbulence levels in the Imperial College supersonic wind tunnel with the $M = 1.4$ nozzle are $u'/u_e = 2.1\%$ and $v'/u_e = 1.3\%$ (Threadgill and Bruce,
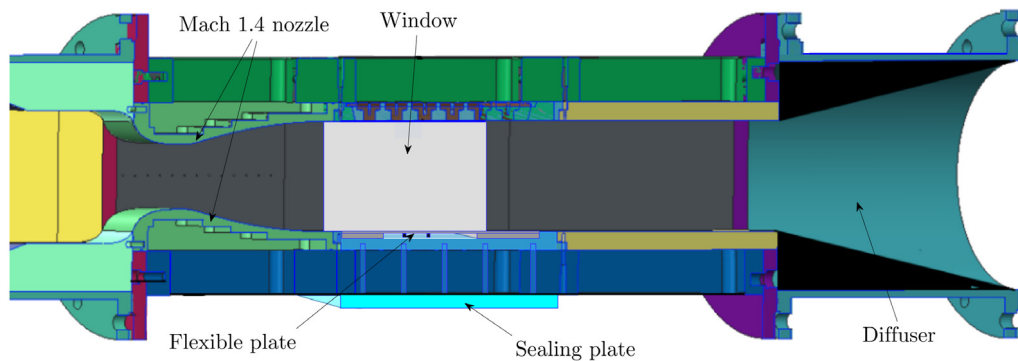
Fig. 3. Imperial College supersonic wind tunnel. *Source:* Figure adapted from Grossman and Bruce (2016).

2015). The average displacement thickness of the boundary layer in the working section was measured to be $\delta^* = 0.91$ mm (Threadgill and Bruce, 2015).

The tunnel is operated via a LabVIEW program consisting of a proportional–integral–derivative (PID) controller that maintains the required stagnation pressure by adjusting the aperture of a pneumatic pressure valve. In order to keep the $M = 1.4$ normal shock in the working section, the tunnel stagnation pressure ratio P_0/P_e is set to 1.278. However, the PID controller leads to low frequency oscillations (≈ 1 Hz) in the tunnel stagnation pressure, hence the requested value is achieved with a standard deviation of 0.16%. Static pressure measurements are obtained using pressure tappings connected to 32 remote pressure transducers sampling at 100 Hz.

2.2. Experimental model

Like most experiments performed on shock control bumps in the past (Bruce and Colliss, 2015), the bump is placed on the wind tunnel floor. This approach facilitates a detailed examination of the flow local to the bump but does not allow straightforward estimation of the drag. Mounting the SCB on a wing model would, in theory, facilitate direct lift and drag measurements, but the very small bump size would lead to a substantial loss of detail. Unlike many previous experiments (Ogawa et al., 2008; Colliss et al., 2014), a shock holding plate is not used, as shock stability is one of the main parameters that is to be assessed in the experiments. The intrinsic wind tunnel unsteadiness (that manifests as low frequency stagnation pressure oscillations) is in fact somewhat representative of the conditions on a transonic wing.

The experimental model tested in the wind tunnel is based on the experiments of Jinks (2016), and is shown in Fig. 4. It consists of a flexible plate representing the bump shape, glued to solid aluminium blocks to facilitate the wind tunnel assembly. Hence, when deployed, the SCB assumes a loaded beam geometry, with no curvature at the two fixed ends. This constraint is especially relevant as it would allow straightforward integration with the material and airframe constraints of current aircraft (Jinks et al., 2014). The plate is made from aluminium alloy Al-7075-T6, material extensively used for aerospace applications, and has dimensions $308 \times 150 \times 0.6$ mm. The free portion of the plate is a square section of $150 \times 150 \times 0.6$ mm. The beginning of the free portion is 40 mm downstream of the leading edge of the flexible plate, and this is marked as $x = 0$ in Fig. 4(b).

The shape of the plate is altered between experiments by an array of LabVIEW-controlled actuators connected to spanwise strips, which ensure a uniform displacement applied across the width of the plate. A 2D bump shape was chosen because of the superior on-design performance when compared to 3D bumps (Eastwood and Jarrett, 2012). The adaptive nature of the SCB tested should mitigate any off-design performance penalty associated with it as its shape can be altered when the flow conditions change. 2D bumps have the additional advantage of allowing bigger deflections to be achieved within the elastic limit. The streamwise location of the actuators (at $x/L = 0.25$ and $x/L = 0.5$) is the result of an optimisation study by Jinks (2016), who used a surface-based performance metric aiming to smear the pressure rise across the shock by considering the pressure gradient over the SCB section.

The experiments presented in this paper focus on the steady state behaviour of the adaptive bump, i.e. the actuators are deployed for the whole length of the run. The transients associated with the deployment and retraction of the bump are not considered. The useful duration of a typical run is approximately 40 s, limited by the capacity of the tanks that store high pressure compressed air, and excluding the start up and shut down periods. As summarised in Table 1, the bumps are tested with a different number of actuation points (0, 1 or 2) and different actuator deployments. Bump heights (h) between 0% and 2% of the bump's length were tested. With respect to the displacement thickness of the incoming boundary layer, this corresponds to $h/\delta^* = 0 - 3.3$. A solid plate is also tested to simulate the flow over a clean aerofoil.

A total of 28 pressure tappings are located on the plate: 18 along the centreline and 10 at $z = \pm 26$ mm. Good agreement between the offset and the centreline pressure profiles (with a mean percentage difference below 2%) indicates that there
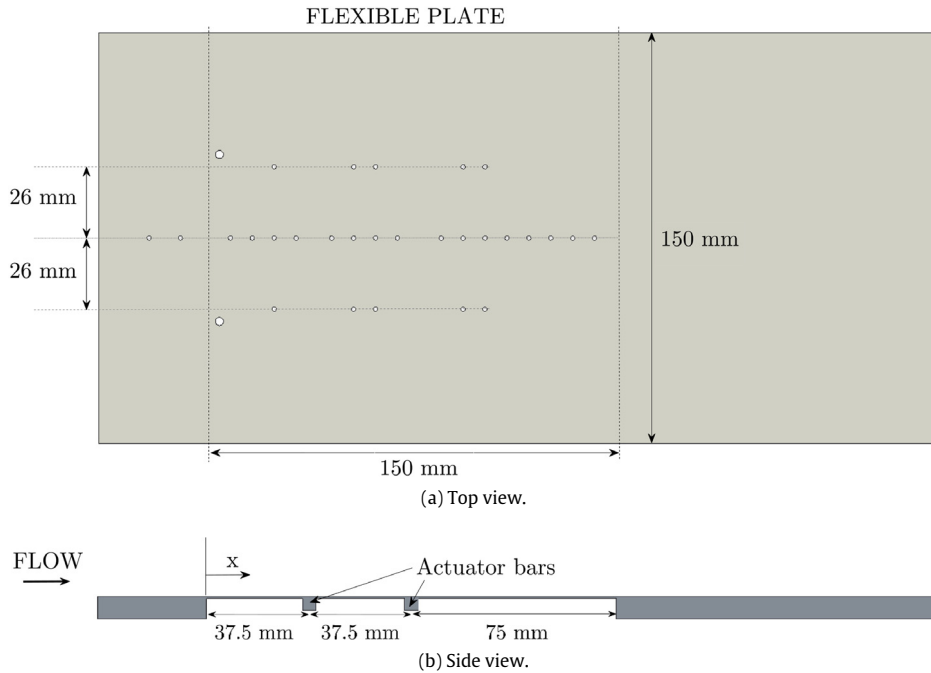
(a) Top view.

(b) Side view.

Fig. 4. Sketches of the flexible plate.

Table 1
Summary of the wind tunnel runs.

Number of actuators	Actuator location		Actuator height		Number of runs	Total time (s)
	(mm)	(/L)	(mm)	(%L)		
0 (solid plate)	–	–	–	–	3	57.7
0 (flexible plate)	–	–	–	–	2	41.4
1	75	0.50	0	0	4	32.3
1	75	0.50	3.0	2.0	3	35.2
2	37.5, 75	0.25, 0.50	0, 0	0, 0	2	36.2
2	37.5, 75	0.25, 0.50	1.1, 1.3	0.7, 0.9	2	25.0
2	37.5, 75	0.25, 0.50	1.7, 2.1	1.1, 1.4	2	51.2
2	37.5, 75	0.25, 0.50	1.7, 2.4	1.1, 1.6	3	62.1

are no strong gradients in the spanwise direction. The cavity below the bump is sealed from the laboratory with a solid aluminium plate, such that the cavity pressure does not change significantly between the runs. However, some air leakage inevitably occurs around the sides of the flexible plate between the test section and the cavity.

2.3. Schlieren photography

Schlieren photography is a flow visualisation technique based on capturing density gradients in the flow through the principle of refracting light (Settles, 2001). A Z-type Schlieren arrangement is chosen with a horizontal knife edge configuration to highlight the negative cross-stream density gradients and the flow features close to the flexible plate. 2048 × 1400 pixel resolution images are recorded at a frame rate of 160 fps and with an exposure time of 40 μs.

High Schlieren accuracy is essential, as incorrect measurements from the Schlieren images could lead to misleading interpretation of results. For this purpose, the square grid in Fig. 5(a) was laser printed on a transparency and fixed in position against the wind tunnel window when the tunnel was not operating in order to assess the accuracy of the setup of the optical system. Isotropy is defined as the ratio of width to height ($\Delta x/\Delta y$) for each square and is used here as a measure to help quantify Schlieren and lens distortion. Fig. 5(b) is an isotropy contour plot for the Schlieren image in Fig. 5(a). It can be seen that isotropy only varies between 0.96 and 1.06, with the values increasing from left to right on the image. As such, the highest errors occur at the edges and the Schlieren image is, fortuitously, most accurate in the central part of the image, especially close to the flexible plate (as shown by the triangle on Fig. 5(b)), i.e. where the lambda shock sits. This allows accurate detection of shock position and plate curvature. The extreme values give a maximum error of 3.7% in the measured angles and 3% in the Mach number calculation when using the expression $\mu = \sin^{-1}(1/M)$.
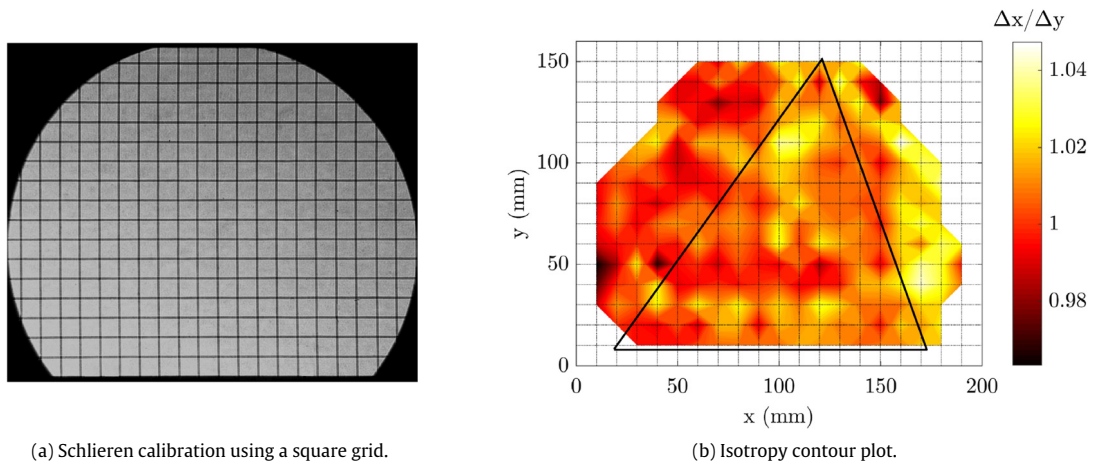
(a) Schlieren calibration using a square grid.   (b) Isotropy contour plot.

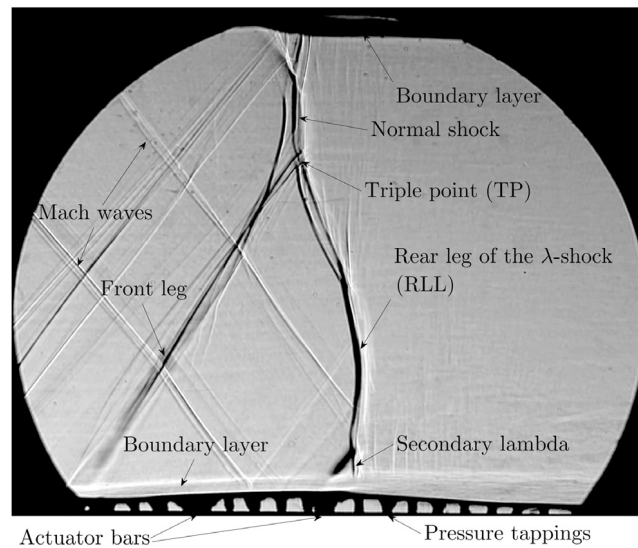**Fig. 5.** Plots showing the effects of optical distortion.

Fig. 6. Annotated Schlieren image for the actuated flexible plate. The $M = 1.4$ bifurcated shock structure is captured with a horizontal knife edge, exposure time of 40 μs and sampling at 160 Hz.
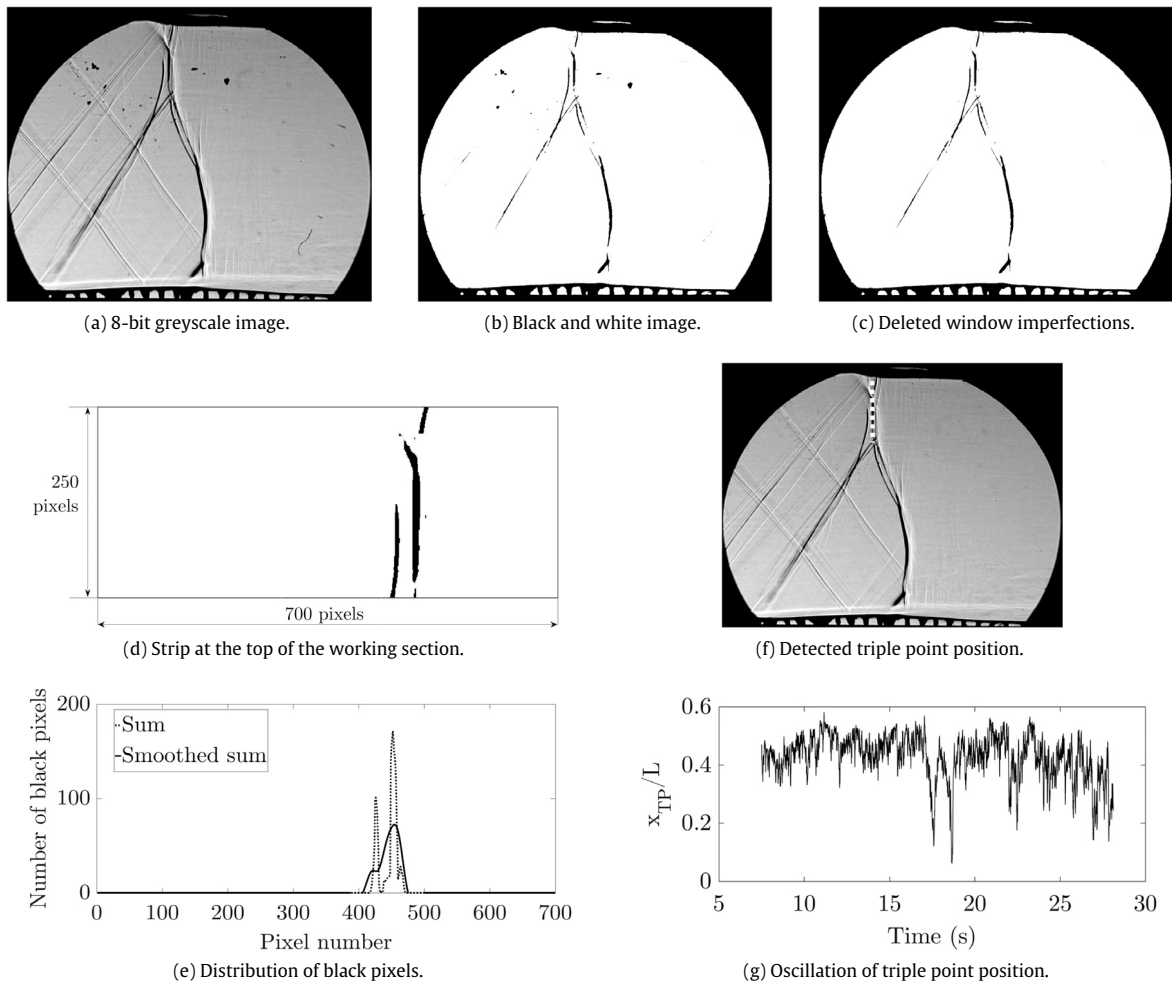
3. Results

It should be noted that all dimensions in this paper have been normalised by bump length ($L = 150$ mm), streamwise distances are measured from the front of the flexible plate, and the bump shapes are labelled according to the displacement of the actuators at $x/L = 0.5$.

3.1. Shock tracking

A typical Schlieren image from the experiments is shown in Fig. 6. Labels indicate the location of the pressure tappings and actuator bars on the flexible plate, boundary layers, Mach waves, and the bifurcated shock structure.

The weak normal shock is bifurcated because the surface curvature at the front of the flexible plate generates compression waves that join up into an oblique shock, leading to the typical lambda shape, with the normal shock, front and rear legs meeting at the triple point (Fig. 6). An additional bifurcation of the rear leg can be observed close to the flexible surface (secondary lambda). The shock wave has a finite thickness on the Schlieren frame due to the spanwise averaging of the Schlieren technique. However, the fact that it is still relatively sharp indicates that the flow can be treated as two-dimensional, as also suggested by the agreement between the centreline and offset pressure profiles.

(a) 8-bit greyscale image.

(b) Black and white image.

(c) Deleted window imperfections.

(d) Strip at the top of the working section.

(f) Detected triple point position.

(e) Distribution of black pixels.

(g) Oscillation of triple point position.

Fig. 7. Example of the triple point detection process for the 1.6% bump.

In order to understand the impact of shock control bumps on wave drag and shock stability, the evolution of shock structure as a function of tunnel stagnation pressure had to be determined. For this reason, tests with a solid plate were performed to establish a baseline test case with an uncontrolled normal $M = 1.4$ shock wave. These tests revealed that the uncontrolled shock wave exhibited considerable unsteadiness due to the small oscillations in tunnel stagnation pressure. When testing flexible plates, the relatively high stiffness of the upstream half of the bump effectively fixed the plate curvature at the leading edge, and consequently also the angle and position of the front leg of the lambda shock, while the rear leg changed its shape and streamwise position as a result of this unsteadiness. To characterise this unsteady behaviour, it is necessary to track the streamwise location of the triple point and the intersection between the rear leg of the λ-shock and the flexible surface.

3.1.1. Triple point

The triple point (TP) position was detected from Schlieren videos. Each video was converted into 8-bit greyscale images (Fig. 7(a)) and, for each frame, the contrast was increased by generating a black and white image (Fig. 7(b)) with a threshold brightness such that all pixels with intensity below 25 were set to 0 and all pixels with intensity above 25 were set to 255. Window imperfections were deleted by subtracting the background image (Fig. 7(c)), and a strip at the top of the working section (700×250 pixels) was considered (Fig. 7(d)). The number of black pixels was added up in the vertical direction, and a locally weighted smoothing scheme ('loess') was implemented in MATLAB, with span equal to 10% of the data (Fig. 7(e)). The streamwise position of the triple point is defined as the location where the smoothed sum of black pixels has a maximum (Fig. 7(f)). The variation of triple point streamwise position over time can be plotted, as per the example plot in Fig. 7(g).

(a) Normalised static pressure (P/P_0) contour.   (b) Mach number contour.
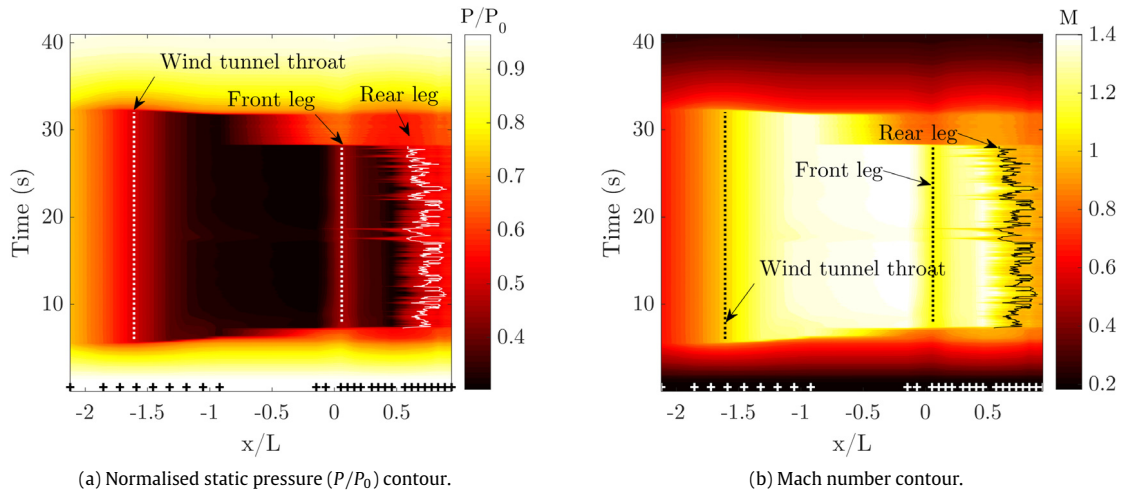
Fig. 8. Example of normalised pressure and Mach number variation with time in the nozzle and on the flexible plate for a 1.6% bump. The crosses mark the positions of the pressure tappings. The approximate locations of the wind tunnel throat, front and rear legs of the lambda shock are marked on the plots.

3.1.2. Rear leg of the λ-shock

The pressure transducers measure static pressure on the side wall of the nozzle and along the centreline of the plate. Fig. 8 shows $x - t$ diagrams of normalised pressure and Mach number in the tunnel during a typical test. It should be noted that the Mach numbers were determined by assuming constant stagnation pressure throughout the working section, equal to the upstream tunnel stagnation chamber pressure. This will inevitably lead to small errors downstream of the shock system. Estimation of the stagnation pressure at the end of the working section from the angle of oblique shocks and Mach waves for the 1.6% bump gives $P_{0,out}/P_{0,in} \approx 0.989$ (compared with a stagnation pressure ratio of 0.958 across a $M = 1.4$ normal shock), leading to a maximum error in the Mach number calculation of less than 0.2%.

The Mach number is seen to increase to $M = 1$ at the throat of the nozzle ($x/L = -1.6$), becoming fully supersonic ($M \approx 1.4$) at the end of the diverging section ($x/L = -0.9$). The curvature of the flexible plate generates the front leg of the lambda shock ($x/L \approx 0$), and shock smearing is demonstrated by the gradual (rather than abrupt) rise in pressure and drop in M in the region $0 < x/L < 0.8$. Flow re-acceleration takes place up until the rear leg of the lambda, after which the flow slows down to subsonic speeds ($M \approx 0.9$).

In order to remove ambiguity from the Schlieren images and ensure consistency between the different frames, the rear leg of the lambda shock is defined as the point where the flow speed is exactly sonic ($M = 1$) according to the normalised wall pressure measurements. It should be noted that care must be taken to interpret results when the shock lies in the region $-0.9 < x/L < -0.2$ (e.g. between 28 and 32 s in Fig. 8), due to the absence of pressure tappings in this region.

3.2. Average profiles

Careful synchronisation of the pressure transducers and Schlieren videos facilitates the study of the variation of shock structure with tunnel stagnation pressure. Fig. 9(a) is a plot of triple point position (measured from Schlieren) as a function of normalised tunnel stagnation pressure for the 1.6% bump. The grey dots represent the 9930 individual data points, which correspond to 62.1 s of data (sampled at 160 Hz to match the Schlieren), compiled from three wind tunnel runs. Fig. 9(b) shows the corresponding position of the rear leg of the λ-shock (RLL) (inferred from static pressure profiles as the point where $M = 1$) against tunnel stagnation pressure.

Statistical data binning can be used to calculate representative mean values and allow easier interpretation of the results. Care must be taken to ensure that the mean values are statistically reliable. Fig. 10(a) shows a convergence plot for the percentage error in the mean triple point position as the number of elements in a representative bin varies (for the 1.6% bump with $P_0/P_e = 1.2840$ and bin width of $P_0/P_e = 0.0005$). It can be seen that the amplitude of the oscillations reduces as the bin size increases. An error of below 5% was deemed acceptable for the purposes of this study. It was determined that 50 samples was the minimum number of samples per bin that could be expected to achieve a percentage error below 5% (4% for the case in Fig. 10(a)), hence it is taken as the threshold value below which the data are discarded. Fig. 10(b) shows the average triple point position against normalised tunnel stagnation pressure, with the black crosses indicating bins that contain more than 50 elements. It can be seen that the profile does not appear smooth outside this range (in particular at lower stagnation pressures), supporting the choice of threshold used in this study.

The crosses in Fig. 9 show the average triple point and RLL positions for the 1.6% bump for a bin width of $P_0/P_e = 0.0005$ for all bins containing at least 50 samples. The same approach is used for the other bump shapes tested. Figs. 11(a) and 11(b)
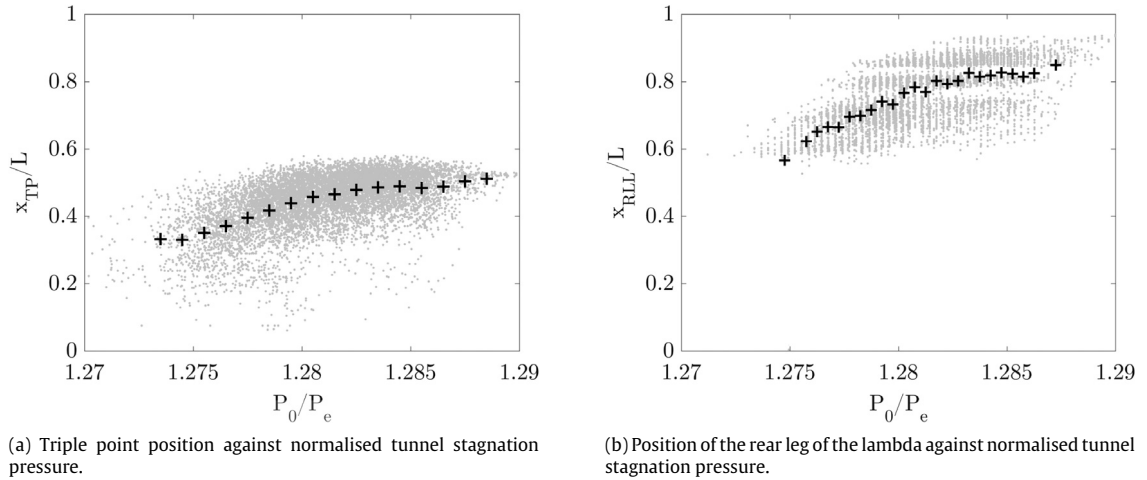
(a) Triple point position against normalised tunnel stagnation pressure.

(b) Position of the rear leg of the lambda against normalised tunnel stagnation pressure.

Fig. 9. Instantaneous (grey dots) and average (black crosses) shock position against normalised stagnation pressure in the tunnel for the 1.6% bump.

(a) Convergence plot for the percentage error in the mean triple point position for the bin with $P_0/P_e = 1.284$.

(b) Mean triple point position against normalised tunnel stagnation pressure. The black crosses correspond to the bins with more than 50 elements.
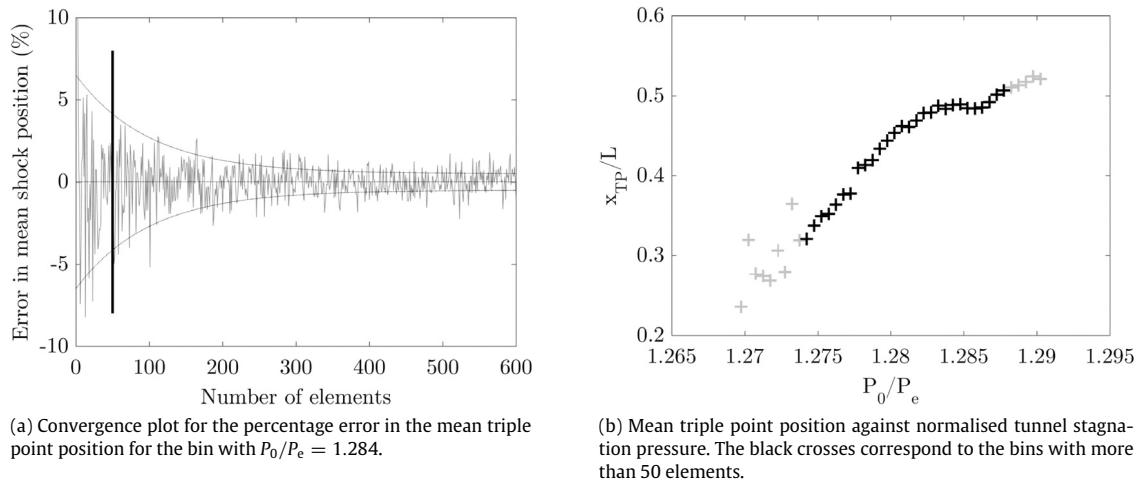
Fig. 10. Convergence plot and mean triple point profile for the 1.6% bump. Bin width: $P_0/P_e = 0.0005$.

are plots of average triple point and RLL positions respectively as a function of normalised tunnel stagnation pressure for all bump geometries investigated. The asterisks correspond to the baseline case (solid plate), while all the other profiles are for flexible bumps as per Table 1. The displacements shown in the legend of Fig. 11 refer to the deployment of the actuators at $x/L = 0.5$.

3.2.1. Shock stability

Shock stability can be assessed from the gradient of the lines in Fig. 11(a): a shallow gradient indicates a more stable shock as the same change in tunnel stagnation pressure leads to a smaller change in normal shock position (represented by the triple point). Fig. 11(a) shows that, in all cases, the bumps stabilise the shock compared with the baseline case. This effect has been reported before (Bruce and Colliss, 2015) and is usually attributed to the anchoring effect of the front leg of the lambda, always generated at the beginning of the flexible surface. In fact, as the inlet stagnation pressure changes (but the exit stagnation pressure stays constant), the change in shape and position of the rear leg modifies the wave drag across the shock system without the need for large normal shock oscillations. This will be discussed further in the next section.

Fig. 11(a) would also seem to suggest that all the bump shapes tested have a similar performance. However, the results plotted in Fig. 11(b) demonstrate significant differences in the λ-shock structure generated by the different bumps.

3.2.2. Wave drag saving

A comparison between the average RLL profiles in Fig. 11(b) provides insight into the wave drag associated with the different bumps. In fact, the Imperial College supersonic wind tunnel exhausts to atmosphere, thus fixing the exit stagnation
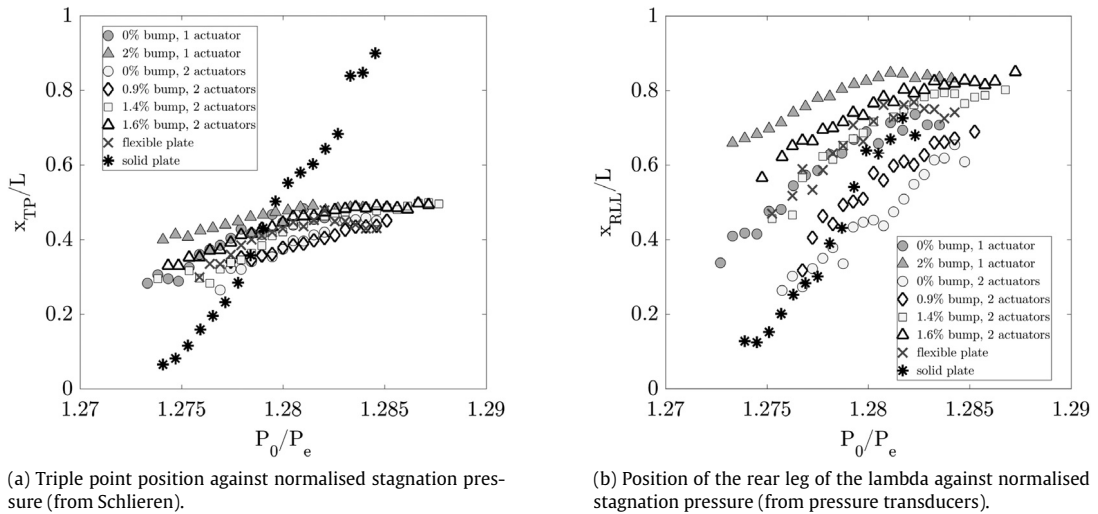
(a) Triple point position against normalised stagnation pressure (from Schlieren).

(b) Position of the rear leg of the lambda against normalised stagnation pressure (from pressure transducers).

Fig. 11. Mean profiles for the triple point position and rear leg of the lambda shock for several bump shapes.
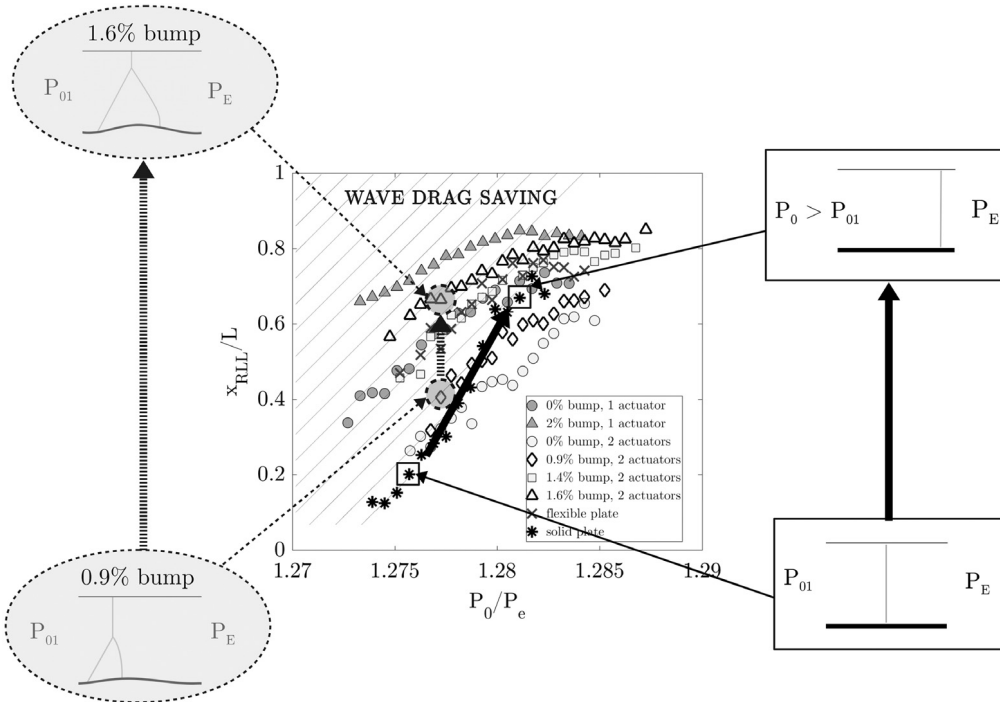

Fig. 12. Annotated plot of RLL position against normalised tunnel stagnation pressure for several bumps and the solid plate.
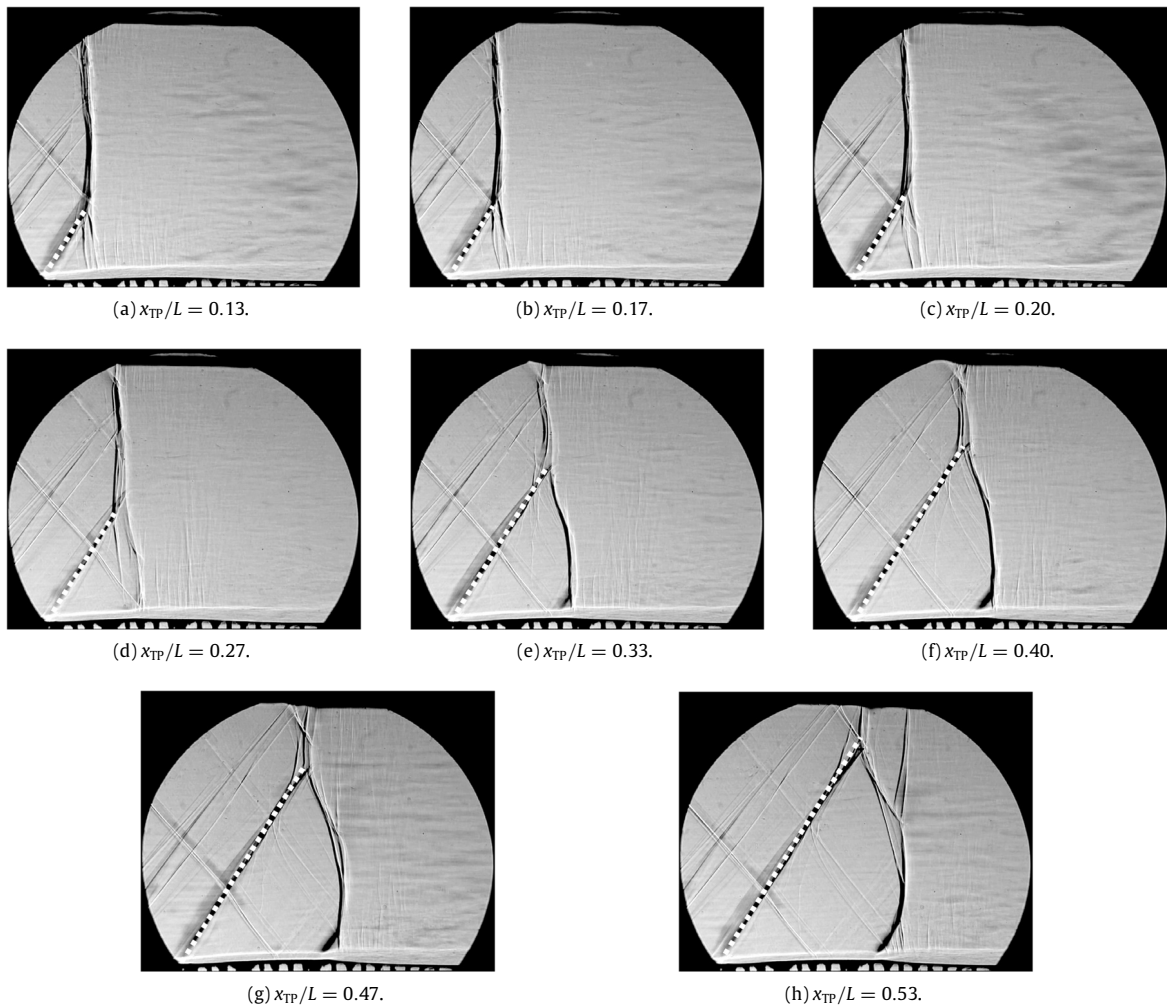
pressure. This implies that the variation in upstream stagnation pressure must be compensated by a change in the losses in the working section, which are composed of viscous drag due to boundary layers and wave drag across the shock. At Mach numbers greater than 1, viscous effects in the boundary layer are more important than in subsonic flows, and lead to larger losses associated with the supersonic region upstream of the shock than with the subsonic portion downstream (Anderson, 1990). Following the solid black arrow on Fig. 12, it can be surmised that, for the solid plate case, as P_{01} increases, the normal shock moves downstream such that larger viscous losses are incurred in the (supersonic) upstream boundary layer, while the wave drag (which is purely a function of upstream Mach number for a normal shock) stays approximately constant. If, however, P_{01} is also fixed, it follows that the overall losses in the working section must be the same between any two cases with the same P_0/P_e (i.e. moving along the dashed arrow on Fig. 12). Given that the position of the front leg of the lambda
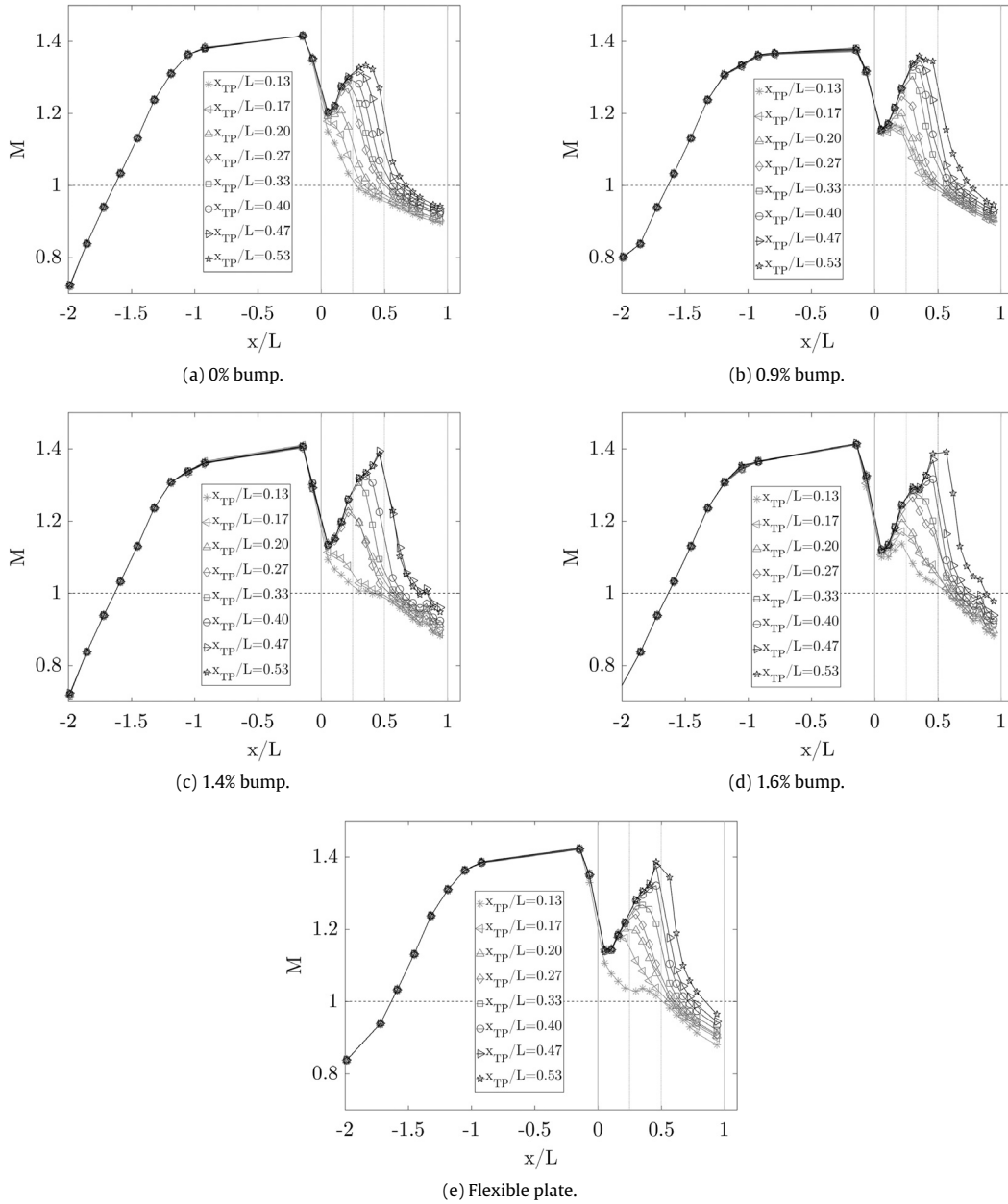
Fig. 13. Mach number profiles for eight different triple point positions for four bump shapes and the flexible plate. On each plot, the darker shades of grey indicate a more downstream triple point.

structure is fixed by the curvature of the flexible plate, the rear leg moving downstream for the 1.6% bump suggests a viscous drag rise, and consequently a wave drag reduction. Hence, the results in Fig. 11(b) suggest that the wave drag associated with the lambda shock falls as the profiles shift upwards. In particular, a wave drag saving compared with the baseline case is observed when the data are above the black asterisks, i.e. in the shaded portion of Fig. 12.

Following this logic, Fig. 12 shows that wave drag savings are only observed at low stagnation pressures, for when the triple point is at the front of the bump, namely more upstream than the crest (which lies at $x/L \approx 0.5$). The reasons for this are explored in Fig. 13, which shows Mach number profiles in the nozzle and on the flexible plate for five bump shapes. In each case, profiles for eight triple point positions ($0.13 \leq x_{TP} \leq 0.53$) are shown. For each triple point position, several instantaneous pressure profiles were averaged in order to obtain a representative Mach number distribution. It should be noted that pressure profiles for triple points more upstream than $x_{TP}/L \approx 0.25$ are provided in Fig. 13 but do not have

(a) $x_{TP}/L = 0.13$. (b) $x_{TP}/L = 0.17$. (c) $x_{TP}/L = 0.20$.

(d) $x_{TP}/L = 0.27$. (e) $x_{TP}/L = 0.33$. (f) $x_{TP}/L = 0.40$.

(g) $x_{TP}/L = 0.47$. (h) $x_{TP}/L = 0.53$.

Fig. 14. Lambda shock structure for the 1.4% bump and different triple point positions. The thick dashed white lines are plotted at 58° on all frames, showing that the angle of the front leg of the λ-shock remains almost constant.
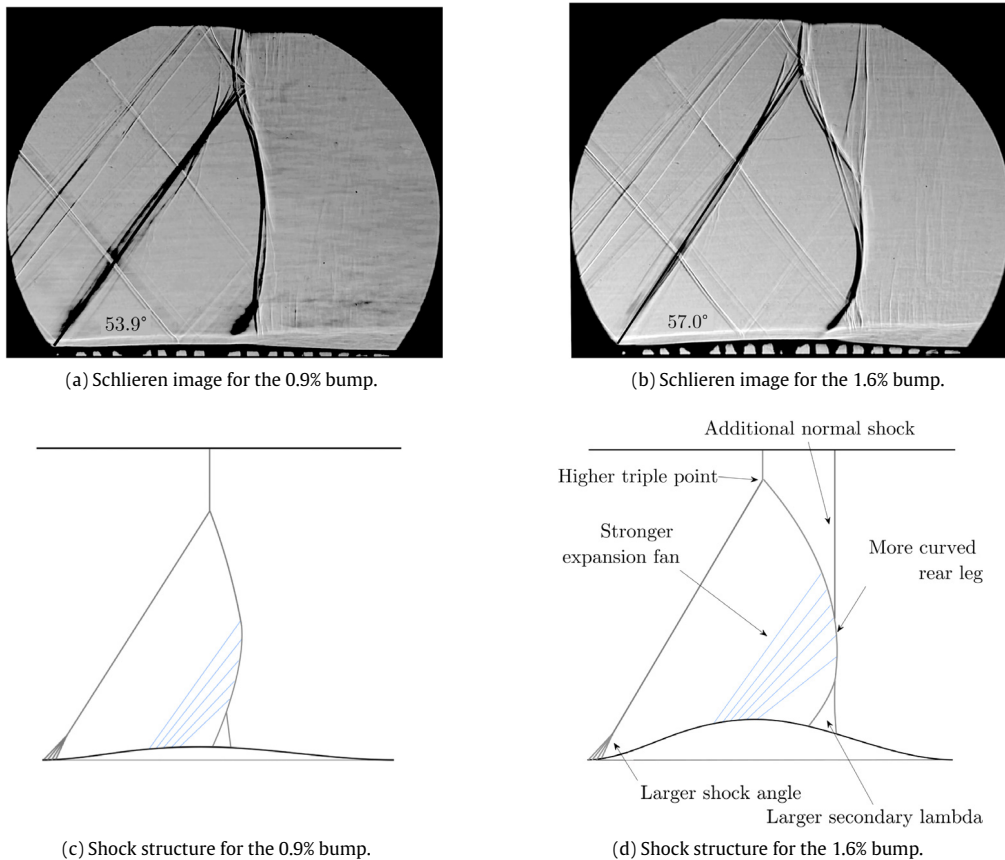
corresponding average points in Fig. 11(a). This is due to the fact that, for the low stagnation pressure ratios required for upstream triple points, there were less than 50 elements per bin (as explained in Section 3.2).

In all the cases, Fig. 13 shows that the flow Mach number drops around $x/L = 0$ due to the effect of the front leg of the lambda. For upstream triple point positions, this is followed by a plateau or moderate flow reacceleration followed by further deceleration, showing evidence of the desirable two-step pressure rise. However, detrimental flow reacceleration is observed for more downstream triple point positions, with peak rear-leg (normal) shock strengths approaching $M = 1.4$ in most cases. While oblique shocks are often near-isentropic even for relatively high Mach numbers, the entropy generation (i.e. wave drag) associated with a normal shock rises rapidly with shock strength. It follows that the wave drag saving due to partial flow recompression through the (more efficient) oblique shock is cancelled by the stagnation pressure drop associated with the rear shock as its strength becomes comparable with that for the baseline case.

The Schlieren images in Fig. 14 show the evolution of the lambda structure for the 1.4% bump as the triple point moves downstream. The angle of the oblique shock (shown as a dashed white line) remains approximately constant at 58°as the normal shock moves, confirming that the surface curvature at the front of the plate is almost independent of shock position.

A significant change in shock structure is observed between Figs. 14(d) and 14(e), where the secondary lambda appears for the first time. This feature then strengthens as the rear leg of the main lambda intersects the flexible plate past the crest of the bump (Figs. 14(f)–14(h)). Consistently, the Mach number profiles in Fig. 13(c) show that the three cases with the most downstream shock position exhibit the strongest flow reacceleration.

Comparison of the performance of the 0%, 0.9%, 1.4%, and 1.6% bumps with two actuation points in Fig. 11(b) reveals how, as the bumps becomes taller, the RLL moves further downstream along the flexible surface. Fig. 15 compares the λ-shock structures for the 0.9% and 1.6% bumps for the same value of P_0/P_e, and shows how this downstream shift is due to the

(a) Schlieren image for the 0.9% bump.

(b) Schlieren image for the 1.6% bump.

(c) Shock structure for the 0.9% bump.

(d) Shock structure for the 1.6% bump.

Fig. 15. Schlieren images and diagrams showing how the shock structure changes for two different actuator displacements for a triple point position of $x/L = 0.53$.

interplay of several factors. Firstly, the greater surface curvature at the front of the flexible plate increases the angle of the front leg of the lambda (from 53.9° for the 0.9% bump to 57.0° for the 1.6% bump), therefore raising the triple point (for the same streamwise position). In addition, the stronger expansion fan (due to the larger convex curvature around the crest) increases the curvature of the rear leg, and an additional normal shock appears to ensure uniform flow conditions. These observations emphasise how very small geometric variations between the two bumps cause very significant changes in the flowfield such that, on average, the taller bumps are associated with larger wave drag savings. The superior total pressure recovery capability of taller adaptive SCBs was highlighted in the computational study by Jinks et al. (2014), and has now been demonstrated experimentally.

The additional normal shock that can be observed in Figs. 14(h), 15(b) and 15(d) ensures uniform flow conditions in the working section and it appears when supersonic flow reacceleration leads to a rear leg of the lambda of $M \approx 1.4$ or stronger. This threshold was calculated assuming that there are no discontinuities in static pressure between the regions above and below the triple point, and is consistent with what was observed from the Schlieren videos (Fig. 14). The interaction of this shock with the upper surface of the wind tunnel inevitably leads to increased viscous losses in the boundary layer. However, the shock is expected to be very weak in all the cases presented in this paper because Fig. 13 shows that the strength of the RLL never exceeds $M = 1.4$, so the additional pressure rise required is small. The detrimental effect on the boundary layer can therefore be considered negligible for the purpose of this study.

Extending the comparison to cases with a different number of actuation points shows that the stiffness of the flexible plate is a crucial factor in determining the performance of the bump. As Jinks (2016) highlighted, one of the main effects of the actuators is to constrain the plate displacement, allowing useful deflections to be achieved, while ensuring suitable levels of stiffness. It follows that decreasing the number of actuation points reduces the stiffness of the plate. In particular, the absence of an actuation point at $x/L = 0.25$ allows greater surface curvatures to be achieved at the front, increasing the angle of the front leg of the lambda shock. This explains why the '0% bump, 1 actuator' and 'flexible plate' mean lines on Fig. 11(b) are shifted upwards compared with the corresponding case with two actuators. In addition, it should be noted that the profiles for the flexible plate in Figs. 11 and 12 are closer to those for the 0% bump with one actuation point than

(a) 0% bump.

(b) 0.9% bump.

(c) 1.4% bump.

(d) 1.6% bump.
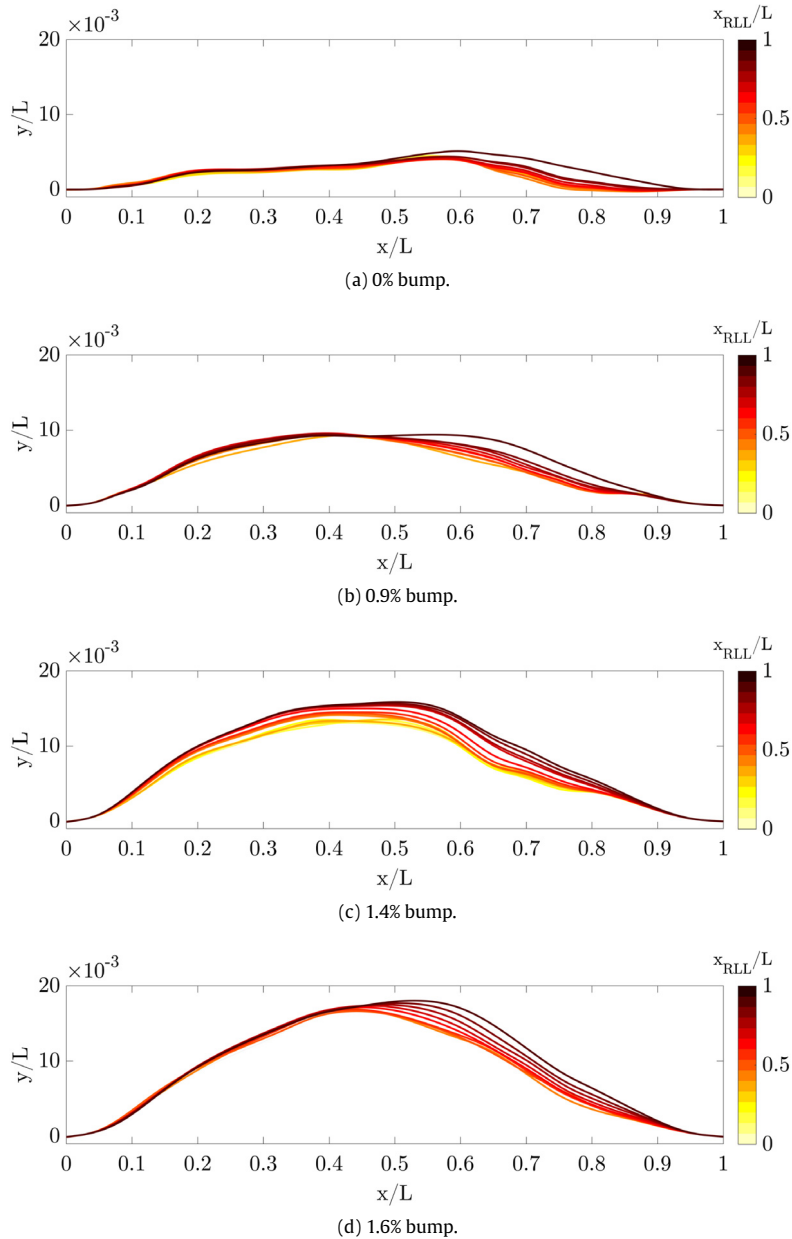
Fig. 16. Variation of average plate shape with RLL position for the bumps with two actuation points.

with two actuation points. In fact, increasing the number of constraints moves the deformed bump shape away from the unconstrained case.

The results presented in Figs. 11(b) and 14 are broadly consistent with previous findings about the sensitivity of (rigid) SCB performance to shock position relative to the bump crest presented in Section 1. However, the previously quantified detrimental effect of a very upstream shock has not been captured as in Fig. 2(a). In fact, the plots in Fig. 13 suggest that in this case the normal shock would not be bifurcated, but some drag savings relative to the solid plate case might still be expected (according to Fig. 11(b)). Ultimately, more data points for upstream triple point positions are needed to draw more meaningful conclusions.

3.2.3. Plate profiles

Fig. 16 shows the qualitative variation of average plate shape with RLL position during a single run for each of the four bumps with two actuation points. The profiles were determined from the Schlieren frames: points were detected on the
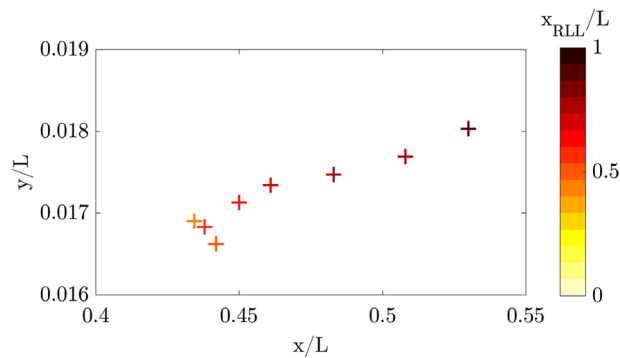
Fig. 17. Location of plate crest as a function of RLL position for the 1.6% bump.

bottom surface of the flexible plate (where the flow is subsonic, in order to minimise the effects of optical distortion), and a smoothing spline (with smoothing factor > 0.999) was fitted through them. The constraint of zero displacement and curvature at the two fixed ends was imposed to obtain more realistic profiles. While this method is effective for Figs. 16(b)–16(d), it shows some limitations for the 0% bump (Fig. 16(a)), as the lack of detected points around $x/L = 0.25$ and 0.5 (due to the presence of the actuator bars, which cast a shadow in the Schlieren images) hampers the accurate reconstruction of the plate profiles.

From Fig. 16 it can be seen that, in all cases, as the RLL moves downstream and the supersonic region on the upper surface of the plate expands, the pressure differential across the plate exerts a force that leads to increasingly positive deformations of the plate into the flow. This trend is particularly evident on the downstream half of the bumps, as the actuation point at $x/L = 0.25$ increases the stiffness of the upstream half and therefore limits vertical deformations.

It should be noted that, although the actuators were deployed with the wind tunnel off and kept in position for the whole duration of the run, Fig. 16 shows some evidence that the actuators (located at $x/L = 0.25$ and 0.5) did move slightly over the course of a test. The maximum displacement of an actuator was observed for a 1.4% test case and was estimated to be 0.6 mm, or 0.4% of the bump length.

Fig. 17 shows the variation of average plate crest location with changes in RLL position for the 1.6% bump. It can be seen that the crest is pulled up and shifted downstream by a downstream motion of the rear leg of the lambda shock. This unique behaviour of these adaptive bumps has a significant impact on performance: as the crest effectively "follows" the RLL, the changes in plate curvature reduce the extent of supersonic reacceleration, therefore weakening the rear leg of the lambda and reducing the associated wave drag. This reduces the sensitivity of the bump's performance to shock position, as the small degree of passive actuation partially compensates for any variations in shock position (i.e. shock unsteadiness). These results broadly agree with previous trends (for solid SCBs), but Figs. 16 and 17 have shown that adaptive SCBs may offer some advantage in comparison to solid bumps with the same shape.

3.3. Statistical distribution of the results

While the results presented in the previous sections highlight the mean trends, this section discusses the statistical distribution of the data. Fig. 18 presents Probability Density Functions (PDF) for the normalised tunnel stagnation pressure, triple point position, and RLL position for the bumps with two actuation points and four different actuator displacements. The mean (μ), standard deviation (σ) and skewness (γ) for the distributions are annotated on each plot.

Fig. 18 shows that the tunnel stagnation pressure distributions are highly consistent between tests with different bumps, all having near-normal distributions symmetric around their means. On the contrary, the triple point position distributions highlight some dissimilarities between the performance of the different bumps, in addition to those discussed in Section 3.2. As the actuators are deployed more, the mean and absolute skewness of the triple point position increase (from 0.38 to 0.45 and from -0.14 to -1.29 respectively), indicating a downstream shift of the triple point, which can also be seen in Fig. 18. In addition, the reduction in standard deviation means that the data move closer to their mean, hence the taller bumps have a greater shock stabilising effect.

It is important to consider these variations in the distributions of triple point position in the context of corresponding RLL distributions. Fig. 18c, 18f, 18i, and 18l indicate that, as the bumps become taller, the mean RLL position increases (from 0.54 to 0.77) and the standard deviation reduces (from 0.13 to 0.09). This means that the RLL moves downstream and is stabilised by an increase in bump height. In addition, Fig. 18 shows that the RLL distributions exhibit a bistable behaviour, with two peaks at $x_{RLL}/L \approx 0.71$ and $x_{RLL}/L \approx 0.85$. These peaks are more evident for the taller bumps, where the mean triple point position is furthest downstream.

This bistable behaviour, which exhibits large-scale fluctuations, as well as small scale oscillations around two equilibrium points, is hypothesised to be related to some sort of complex coupling between aerodynamic and structural instabilities.
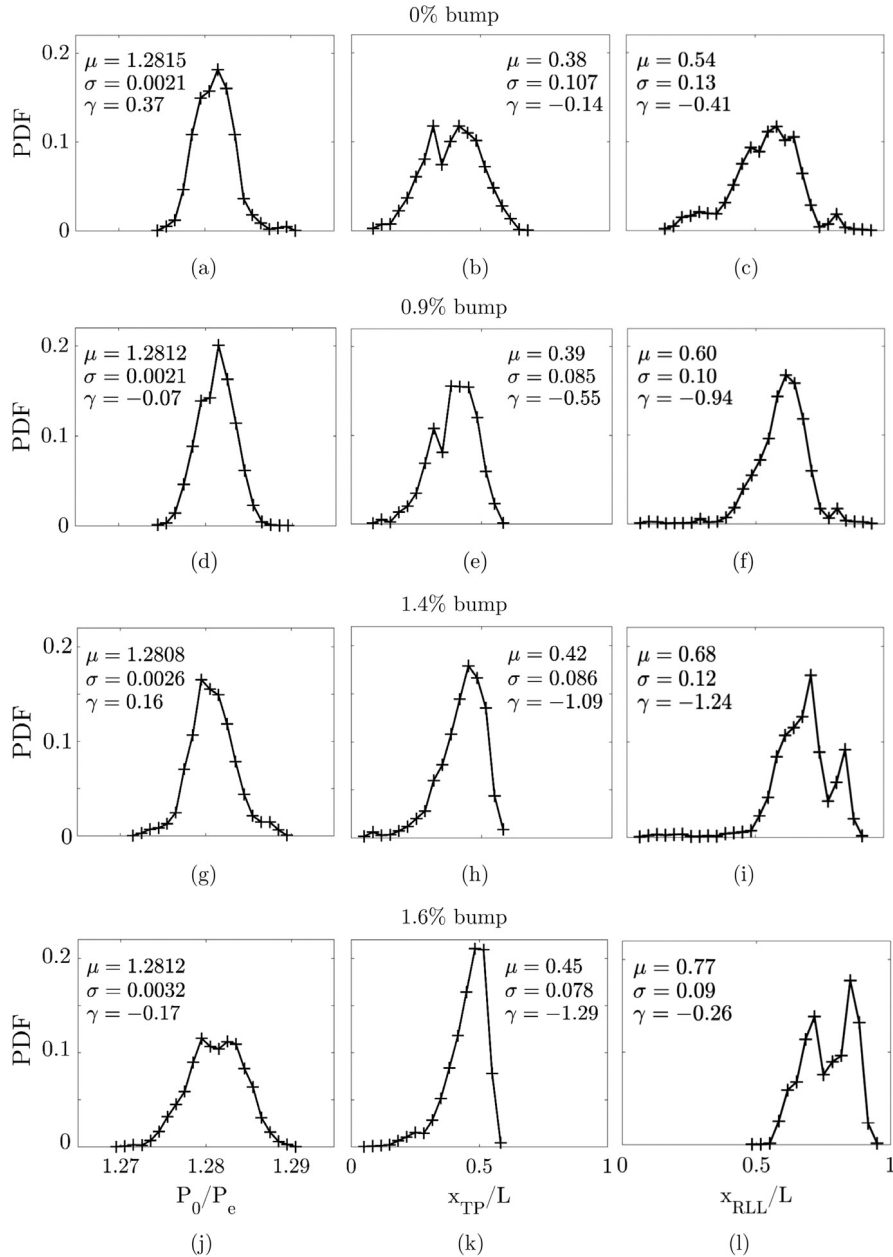
Fig. 18. Probability density functions (PDF) for the normalised tunnel stagnation pressure, triple point and RLL position for the bumps with two actuation points. The mean (μ), standard deviation (σ) and skewness (γ) for the distributions are annotated on the plots.

Two phenomena that bear a close resemblance to the bistability observed in this study are the instability associated with beneficial flow control, identified by Ogawa and Babinsky (2006), and snap-through buckling (Zdeněk and Cedolin, 2003) of the downstream half of the flexible plate. Further work will be carried out to fully understand the mechanisms involved.

4. Conclusions

Experiments have been performed in the Imperial College supersonic wind tunnel at Mach 1.4 to study the shock stabilisation and wave drag reduction potential of a 2D adaptive shock control bump. The bump is modelled as a flexible aluminium alloy plate deformed by uniform spanwise actuation, and static pressure tappings are located along its centreline. With this novel experimental setup, Schlieren images and pressure readings for several bump shapes have been analysed to determine the variation in the average λ-shock structure with stagnation pressure in the tunnel.

Results show that all the bumps tested reduce shock unsteadiness, and an explanation for this reduction is proposed that relates the shock motion to the wave drag associated with the shock system. Wave drag was found to be highly dependent on the shock position relative to the crest of the bump, and a wave drag saving was only observed when the shock was on the upstream portion of the flexible plate. For more downstream shock positions, flow reacceleration leads to a stronger rear shock, and hence an increase in wave drag. It was found that, on average, taller bumps lead to larger wave drag savings due to the greater surface curvature at the front of the flexible plate. Taller bumps also exhibit a greater shock-stabilising effect.

A study of the variation of average plate shape with RLL position shows positive deformations of the downstream half of the adaptive bump as the RLL moves downstream. This small degree of passive actuation means that the position of the crest partially follows the rear leg of the lambda shock, therefore limiting the extent of supersonic reacceleration, the strength of the rear shock, and the wave drag associated with it. This highlights the promising potential of adaptive SCBs to offer higher levels of robustness to small variations in shock positions, compared with solid bumps with the same geometry.

Although the study presented in this paper was done for devices perpendicular to unswept flow, previous results (Birkemeyer et al., 2000; Kutzbach et al., 2004) have shown that the performance of 2D bumps is not significantly different for swept wing cases. This suggests that 2D adaptive SCBs can have a realistic application on transonic aerofoils. In addition, adaptive bumps could be employed in supersonic intakes. This work suggests that they could be beneficial to mitigate the effects of the terminal normal shock instead of a bleed system, and research is ongoing at Imperial College to determine the features of a reflected SBLI between an oblique shock and a flexible surface (Tan, 2017).

The position of the RLL exhibits a bistable behaviour, showing evidence of two local equilibrium points with an instability region in between. This phenomenon is particularly evident for the taller bumps tested and is thought to be caused by a complex coupling of different mechanisms. Aerodynamic (i.e. instabilities associated with beneficial flow control) and structural (i.e. snap-through buckling) mechanisms may offer some insight into the observed behaviour, but further work is required to gain a more complete understanding. Future research will focus on improving the fidelity of the control of the plate curvature to reduce the dependency of the bump's performance on shock position.

Acknowledgement

References

Anderson, J.D., 1990. Modern Compressible Flow: with Historical Perspective. McGraw-Hill New York.

Birkemeyer, J., Rosemann, H., Stanewsky, E., 2000. Shock control on a swept wing. Aerosp. Sci. Technol. 4 (3), 147–156.

Bruce, P.J.K., Colliss, S.P., 2015. Review of research into shock control bumps. Shock Waves 25 (5), 451–471.

Colliss, S.P., Babinsky, H., Nübler, K., Lutz, T., 2014. Joint experimental and numerical approach to three-dimensional shock control bump research. AIAA J. 52 (2), 436–446.

Eastwood, J.P., Jarrett, J.P., 2012. Toward designing with three-dimensional bumps for lift/drag improvement and buffet alleviation. AIAA J. 50 (12), 2882–2898.

Grossman, I.J., Bruce, P.J.K., 2016. Effect of confinement on shock wave-boundary layer interactions in rectangular intakes. In: 54th AIAA Aerospace Sciences Meeting, San Diego, California, pp. 348–367.

Jinks, E., 2016. Adaptive Shock Control Bumps (Ph.D. thesis), Imperial College London.

Jinks, E., Bruce, P.J.K., Santer, M., 2014. Adaptive shock control bumps. In: 52nd Aerospace Sciences Meeting, National Harbor, Maryland, pp. 945–960.

Jones, N.R., Eastwood, J.P., Jarrett, J.P., 2016. Adapting three-dimensional shock control bumps for swept flows. AIAA J. 55 (3), 861–873.

König, B., Pätzold, M., Lutz, T., Krämer, E., Rosemann, H., Richter, K., Uhlemann, H., 2009. Numerical and experimental validation of three-dimensional shock control bumps. J. Aircr. 46 (2), 675–682.

Kutzbach, M., Lutz, T., Wagner, S., 2004. Investigations on shock control bumps for infinite swept wings. In: 2nd AIAA Flow Control Conference, pp. 2702–2712.

Ogawa, H., Babinsky, H., 2006. Experimental investigation of 3D shock/boundary layer interaction control in transonic flows. In: 44th AIAA Aerospace Sciences Meeting and Exhibit, Reno, Nevada, pp. 879–891.

Ogawa, H., Babinsky, H., Pätzold, M., Lutz, T., 2008. Shock-wave/boundary-layer interaction control using three-dimensional bumps for transonic wings. AIAA J. 46 (6), 1442–1452.

Rhodes, O., Santer, M., 2011. Structural optimization of a morphing shock control bump. In: The Proceedings of 52nd AIAA/ASME/ASCE/AHS/ASC Strutures, Strutural Dynamics and Materials Conference, Denver, Colorado, pp. 2129–2147.

Settles, G.S., 2001. Schlieren and Shadowgraph Techniques: Visualizing Phenomena in Transparent Media, Vol. 1. Springer.

Tan, S.S., 2017. Oblique Shock/Boundary Layer Interaction on a Flexible Surface (Master's thesis), Imperial College London.

Threadgill, J.A.S., Bruce, P.J.K., 2015. Unsteadiness in shock wave boundary layer interactions across multiple interaction configurations. In: 53rd AIAA Aerospace Sciences Meeting, pp. 1977–1994.

Zdeněk, P.B., Cedolin, L., 2003. Stability of Structures: Elastic, Inelastic, Fracture and Damage Theories. Dover Publications, Inc.